Single-Stage Three-Phase Current-Source Photovoltaic Grid-Connected Inverter High Voltage Transmission Ratio

Daolian Chen, *Senior Member, IEEE*, Jiahui Jiang, Yanhui Qiu, Jie Zhang, and Fusong Huang

***Abstract*—This paper proposes a circuit topology of a single-stage three-phase current-source photovoltaic (PV) grid-connected inverter with high voltage transmission ratio (VTR). Also, an improved zone sinusoidal pulsewidth modulation (SPWM) control strategy and an active-clamped subcircuit that can suppress the energy storage switch's turn-off voltage spike are introduced. The circuit topology, control strategy, steady principle characteristics, and high-frequency switching process are analyzed profoundly, as well as the VTR's expression and design criterion of the center-tapped energy storage inductor. The improved zone SPWM control strategy consists of two control loops, namely, the outer loop of input dc voltage of PV cells with the maximum power point tracking and the inner loop of the energy storage inductor current. The experimental results of a 3-kW 96VDC/380V50Hz3φAC prototype have shown that this kind of a three-phase inverter has the excellent performances such as single-stage power conversion, high VTR and power density, and high conversion efficiency. Nonetheless, it has small energy storage inductor and output *CL* filter, low output current total harmonic distortion, and flexible voltage configuration of the PV cells. This study provides an effective design method for single-stage three-phase inverting with high VTR.**

***Index Terms*—Current source, high voltage transmission ratio (VTR), photovoltaic (PV) grid-connected inverter, three-phase, zone Sinusoidal Pulse width modulation (SPWM) control strategy.**

I. Introduction

AT PRESENT, the photovoltaic (PV) grid-connected power generation systems commonly adopt the voltage source circuit, which requires the value of dc voltage higher than the peak value of ac voltage. Therefore, an obvious defect arises. When the output capability of the PV cells weakens, i.e., in rainy day or at night, the operation of the whole system stops, along with the decrease of its utilization rate [1]–[6].

PV cells operate as current source, therefore, the current-source inverter (CSI) is more suitable for the PV power generation system. Compared with the voltage-source inverter, the CSI has the following characteristics [7]–[17]:

1) boosting feature, the input dc current can be manipulated by controlling the magnetizing time of the energy storage inductor, so as to realize the whole process of light utilization from weak to strong;
2) direct control of the output current, thus it is more convenient and reliable to realize maximum power point tracking (MPPT), yet the voltage source inverter can cause a dc bus crash and the reliability is accordingly reduced;
3) inductor as the energy storage component, thus the system operation time is longer than that of the voltage source inverter, which uses the electrolytic capacitor as energy storage component;
4) timely protection for overcurrent, which provides a high reliability.

The single-stage three-phase current-source PWM inverter with low voltage transmission ratio (VTR) proposed in [12]–[17] has the advantages of single-stage power conversion, boosting feature, and timely overcurrent protection, but there still exists the flaws. The VTR is not high enough, and the output waveform quality and conversion efficiency will be seriously affected when the input voltage is too low or the input voltage variation range is too wide. For example, a 120–200VDC/380V50Hz3φAC inverter can be achieved, but when the input voltage is lower than 120 V, the duty ratio D is close to the limit value, 1–D is too small, thus the adjusting range of D is limited. This would cause some problems such as poor dynamic characteristics, decrease of the VTR caused by the circuit parasitic parameters, large energy storage inductor current and circuit loss, low conversion efficiency, and worse output waveform. Therefore, it is difficult to invert for low voltage of the PV cells.

In order to overcome the limitations of the traditional voltage source PWM inverter [1]–[6] and single-stage three-phase current-source PWM inverter with low VTR [12]–[17], this paper proposes a single-stage three-phase CSI with high VTR, as well as the circuit topology and an improved zone sinusoidal pulsewidth modulation (SPWM) control strategy with two control loops. The loops are consisted of the outer loop of input dc voltage with MPPT and the inner loop of the storage inductor current. Besides, an active-clamped subcircuit that can suppress the energy storage switch's turn-off voltage spike is discussed in this paper, with important conclusions obtained.

Manuscript received February 28, 2016; revised June 18, 2016 and September 19, 2016; accepted October 24, 2016. Date of publication November 2, 2016; date of current version May 9, 2017. This work was supported by the Key Project of Natural Science Foundation of China, under Grant 51537001. Recommended for publication by Associate Editor Prof. M. Vitelli.

The authors are with the Fujian Key Laboratory of New Energy Generation and Power Conversion, Fuzhou University, Fuzhou 350116, China (e-mail: chendaolian@hotmail.com; fzujiangjiahui@sina.com; qyh522@sina.com; eezhangjie@163.com; forrest945@163.com).

Color versions of one or more of the figures in this paper are available online at http://ieeexplore.ieee.org.

Digital Object Identifier 10.1109/TPEL.2016.2622722

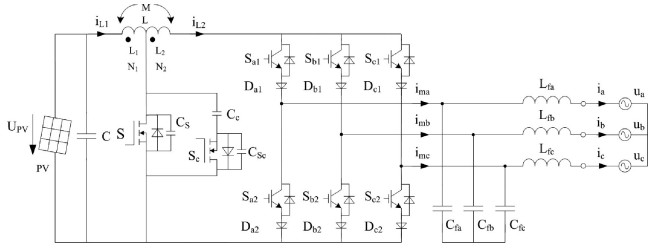

Fig. 1. Circuit topology of a single-stage three-phase current-source PV grid-connected inverter with high VTR.

II. Circuit Topology and Control Strategy

A. Control Strategy

The circuit topology of a single-stage three-phase current-source PV grid-connected inverter with high VTR is shown in Fig. 1. The circuit topology is sequentially cascaded by the input filter capacitor *C*, the center-tapped energy storage inductor *L*, three-phase inverting bridge with six serial blocking diodes and an output *CL* filter. An energy storage switch *S* is connected between the center tap of *L* and the negative end of the PV cells, the left and right turns number of *L* are N_1 and N_2, respectively. Compared to CSI with low VTR [12]–[17], a center tap of the energy storage inductor and an energy storage switch are added to the proposed CSI.

An active-clamped subcircuit connected in parallel at both ends of *S* shown in Fig. 1 is proposed, in order to suppress the turn-off voltage spike of *S*, which is caused by the leakage inductor of L_1. The active-clamped subcircuit is consisted of active-clamped switch S_c and a serial clamping capacitor C_c.

The VTR of the proposed CSI depends on both the energy storage duty ratio and the center tap position of *L*, and it provides a possibility to realize high VTR inverting.

B. Two-Loop Improved Zone SPWM Control Strategy

1) Improved Zone SPWM Control Strategy: An improved zone SPWM control strategy is proposed in the single-stage three-phase current-source PV grid-connected inverter with high VTR. The reference signal that has the same frequency but different in phase of θ with the grid voltage is divided into six 60° intervals in a line cycle by the zero crossing point, thus there exist only two line voltages that is always $\geq \sqrt{6}/2\ U_p$ in every 60° interval, where U_p is root mean square (RMS) value of the phase voltage. This control strategy can ensure the normal operation of the CSI in any high-frequency (HF) switching period with the condition that output line voltage are not smaller than input voltage, i.e., $\sqrt{6}/2\,U_p \geq U_{\mathrm{PV}}$, and obtain high quality of the output grid-connected current.

Set the three-phase grid voltage u_{a}, u_{b}, and u_c as

$$\begin{cases} u_a = \sqrt{2}U_p \sin(\omega t + \theta) \\ u_b = \sqrt{2}U_p \sin(\omega t - 2\pi/3 + \theta) \\ u_c = \sqrt{2}U_p \sin(\omega t - 4\pi/3 + \theta). \end{cases} \tag{1}$$

Three-phase reference signals e_a, e_b, and e_c, which have the same frequency but phase difference of θ with the grid voltages

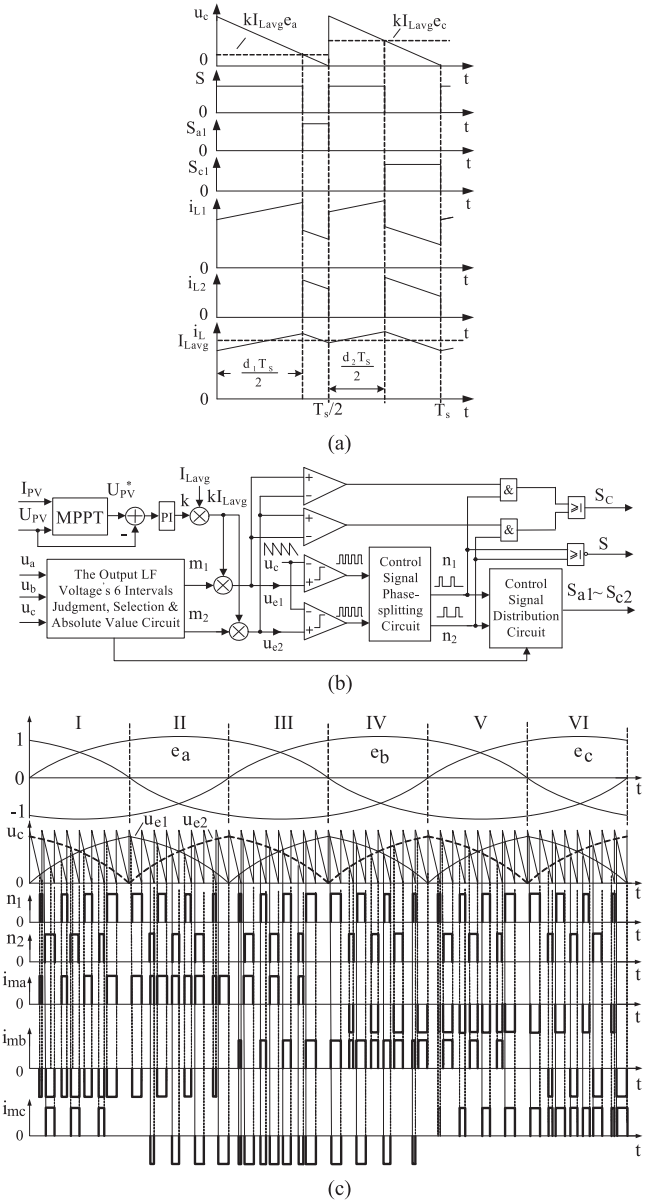

Fig. 2. Two-loop improved zone SPWM control strategy. (a) Generating of control signals in Interval I (b) Zone control diagram (c) Control principle waveforms.

u_a, u_b, and u_c are, respectively, given by

$$\begin{cases} e_a = \sin(\omega t) \\ e_b = \sin(\omega t - 2\pi/3) \\ e_c = \sin(\omega t - 4\pi/3). \end{cases} \tag{2}$$

The aforementioned equation can also be expressed as Fig. 2(c).

The improved zone SPWM control strategy needs to judge the intervals in a line cycle first. The control signals of power switches in different intervals should match Table I in order to ensure the normal operation condition of the CSI in any HF switching period.

From Table I, it can be seen that the operating modes of the inverter are also different in different 60° intervals. Taking

TABLE I
CONTROL SIGNALS OF THE POWER SWITCHES IN DIFFERENT INTERVALS

Interval \ Signal	m_1	m_2	S_{a1}	S_{a2}	S_{b1}	S_{b2}	S_{c1}	S_{c2}	S
I	e_a	e_c	n_1	0	0	1	n_2	0	$\overline{n_1+n_2}$
II	$-e_b$	$-e_c$	1	0	0	n_2	0	n_2	
III	e_b	e_a	n_1	0	n_2	0	0	1	
IV	$-e_c$	$-e_a$	0	n_2	1	0	0	n_1	
V	e_c	e_b	0	1	n_1	0	n_2	0	
VI	$-e_a$	$-e_b$	0	n_1	0	n_2	1	0	

the Interval I as an example, S_{b2} is ON, S_{a2}, S_{b1}, and S_{c2} are OFF, and the power switches S, S_{a1}, and S_{c1} are SPWM modulated, as shown in Fig. 2(a). In Fig. 2(a), *k* is the sampling coefficient of the energy storage inductor current i_L, and $I_{L\mathrm{avg}}$ is the average value of i_{L} in one HF switching period T_S, $T_{\mathrm{S}}/2$ is the sawtooth carrier wave period. The control signals of *S* and S_{a1} are generated by comparing the modulation signal $kI_{L\mathrm{avg}}e_a$ with the former switching period sawtooth wave u_{c}, whereas the control signals of *S* and S_{c1} are generated by comparing the modulation signal $kI_{L\mathrm{avg}}e_c$ with the latter switching period u_c.

2) Two-Loop Improved Zone SPWM Control Strategy: Two-loop improved zone SPWM control strategy of input dc voltage in outer loop and energy storage inductor current in inner loop is adopted in the proposed three-phase grid-connected inverter, as shown in Fig. 2(b) and (c).

The grid-connected current reference signals e_a, e_b, and e_c obtained by sampling the grid voltage u_a, u_b, and u_c have phase difference θ with the grid voltage. The energy storage inductor current signal $i_L = (i_{L1} + N_2/N_1 i_{L2})$ is obtained through sampling the energy storage inductor current i_{L1} and i_{L2}, while i_{L2} converted to i_{L1} to guarantee the continuity of the sampled current in one switching period. By detecting the output voltage U_{PV} and output current I_{PV} of PV cells, maximum power point (MPP) voltage is set as the reference voltage U^*_{PV} of PV cells through MPPT calculation. The difference value of the U^*_{PV} and U_{PV} is amplified to get signal *k*, the average value $I_{L\mathrm{avg}}$ is obtained by sampling i_L once every switching period. Through the output low-frequency (LF) voltage's six intervals judgment, selection and absolute value circuit according to Table I, signals m_1 and m_2 of the corresponding interval are obtained. m_1 and m_2 are, respectively, multiplied by $kI_{L\mathrm{avg}}$ to generate two modulation wave signals $u_{e1} = kI_{L\mathrm{avg}}m_1$, $u_{e2} = kI_{L\mathrm{avg}}m_2$, then they are, respectively, compared with the sawtooth carrier wave u_c to obtain the SPWM control signals of this interval. Signals n_1 and n_2 of the power switches are obtained after the signal phase-splitting circuit because the frequency of the energy release switches is half the frequency of the carrier wave, and then, the signals of the energy storage switch S and the energy release switches of the three-phase inverting bridge are obtained by the signal distribution circuit according to Table I.

III. STEADY PRINCIPLE

A. LF Mode Analysis

There are six operating intervals in a line cycle of the inverter, and each interval can be divided into three operating modes.

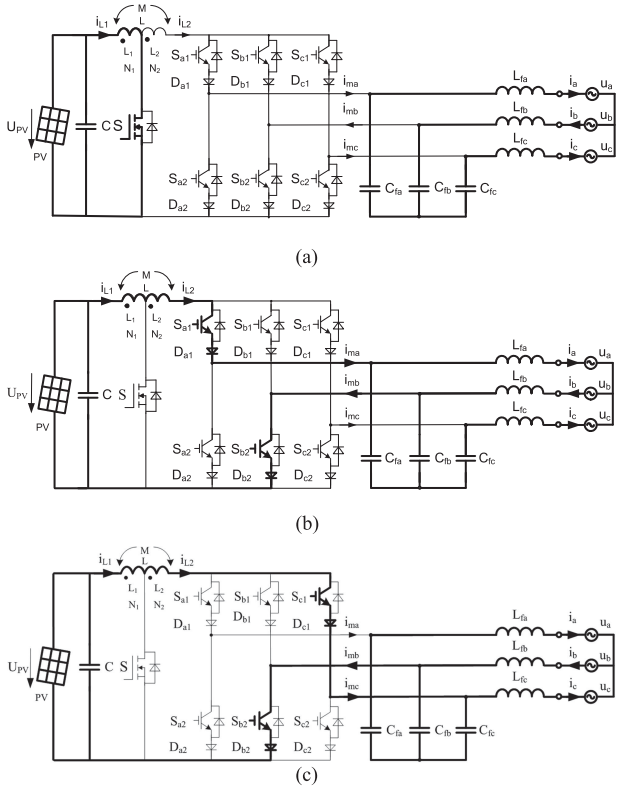

Fig. 3. Operating modes of the inverter in Interval I. (a) S ON, S_{a1}, S_{c1} OFF, (b) S_{a1} ON, S and S_{c1} OFF, (c) S_{c1} ON, S and S_{a1} OFF.

Taking the Interval I in the Table I as an example, three operating modes of the inverter are shown in Fig. 3, when S_{b2} is ON, S_{a2}, S_{c2}, and S_{b1} are OFF.

Mode I-1: S is ON, S_{a1} and S_{c1} are OFF. Energy is stored to L_1 and i_{L1} increases linearly with the rate of U_{PV}/L_1 via the path of U_{PV}, L_1, and *S*. i_a, i_b, and i_c are maintained by C_{fa}, C_{fb}, and C_{fc}.

Mode I-2: S_{a1} is ON, *S* and S_{c1} are OFF. Since $u_{ab} > U_{\mathrm{PV}}$, i_L decreases linearly at the rate of $(u_{ab} - U_{\mathrm{PV}})/L$ via the path of U_{PV}, *L*, and S_{a1}. U_{PV} and *L* deliver energy to the grid simultaneously. i_c is maintained by C_{fc}.

Mode I-3: S_{c1} is ON, S and S_{a1} are OFF. Since $u_{cb} > U_{\mathrm{PV}}$, i_{L} decreases linearly with the rate of $(u_{cb} - U_{\mathrm{PV}})/L$ via the path of U_{PV}, *L*, and S_{c1}, U_{PV} and *L* deliver energy to the grid simultaneously. i_a is maintained by C_{fa}.

In a line cycle, the sequence of operating intervals for the inverter is I–VI, where the sequence of operating modes in Interval I is I–1, I–2, I–1, and I–3. Sequence of operating modes in other intervals is similar.

B. VTR

1) Steady-State Solution of the State Variable: By neglecting the commutation overlap time of the power switches, the magnetizing and demagnetizing switching state equivalent circuits of the inverter are shown in Fig. 4, where the energy storage inductor current is in continuous conduction mode (CCM). In Fig. 4, r_1 is the equivalent resistance including the internal resistance of the input source, the parasitic

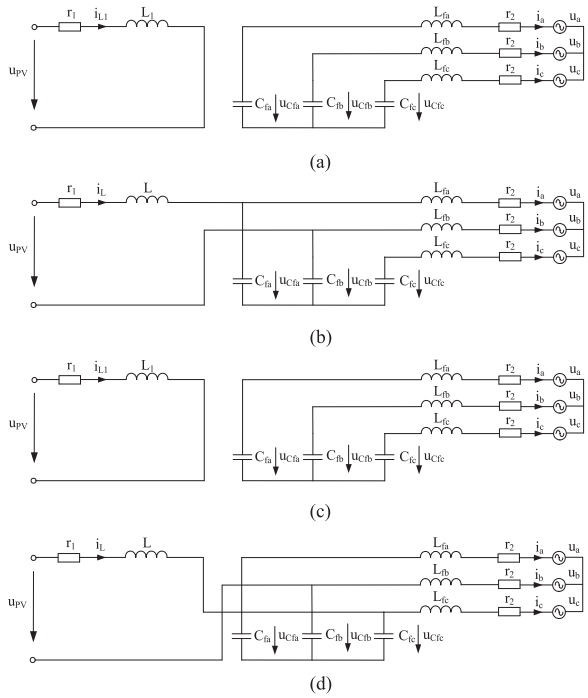

Fig. 4. Switching state equivalent circuits of the inverter in CCM mode. (a) $0\sim d_1T_s/2$ Magnetizing Period, (b) $d_1T_S/2\sim T_s/2$ Demagnetizing Period, (c) $T_s/2\sim(d_2+1)T_s/2$ Magnetizing Period, (d) $(d_2+1)T_s/2\sim T_s$ Demagnetizing Period.

resistance of the energy storage inductor, the on-resistance of the power switches and blocking diodes; r_2 is the equivalent resistance including the internal resistance of the ac grid, and the parasitic resistance of the output filtering inductor; $L = L_1 + L_2 + 2M$, where $M = k'\sqrt{L_1 L_2}$ is the mutual inductor between L_1 and L_2, k' is the coupling coefficient. When $k' = 1$, $L = (\sqrt{L_1} + \sqrt{L2})^2 = L_1[(N_1 + N_2)/N_1]^2$.

In steady state, the magnetizing and demagnetizing of the energy storage inductor basically reach balance, same as the charge and discharge of the capacitor within one T_S, thus the state-space averaging method can be used to obtain the steady-state solution. By multiplying the state equations of Fig. 4(a) by $d_1/2$ plus multiplying the state equations of the Fig. 4(b) by $(1-d_1)/2$ plus multiplying the state equations of Fig. 4(c) by $d_2/2$ plus multiplying the state equations of Fig. 4(d) by $(1-d_2)/2$, with $i_L = i_{L1}N_1/(N_1+N_2)$ substituted, the steady-state solution of the state variables is derived as equation (3) as shown at the bottom of the page.

2) VTR: Considering $r_2 = 0$, following equation is derived from (3)

$$\begin{aligned} r_1\left[\frac{d_1}{2}\left(\frac{N_1+N_2}{N_1}\right)^2+\frac{1-d_1}{2}\right. & \\ \left.+\frac{d_2}{2}\left(\frac{N_1+N_2}{N_1}\right)^2+\frac{1-d_2}{2}\right] i_L & \\ = \left(1+\frac{N_2}{N_1}\frac{d_1+d_2}{2}\right)U_{\rm PV} - \frac{1-d_1}{2}u_a & \\ +\frac{2-d_1-d_2}{2}u_b - \frac{1-d_2}{2}u_c & \quad (4a) \end{aligned}$$

$$\frac{i_a}{i_c} = \frac{1-d_1}{1-d_2} = \frac{\sin(\omega t)}{\sin(\omega t - 4\pi/3)} \quad (4b)$$

$$\frac{i_a}{i_b} = \frac{1-d_1}{d_1+d_2-2} = \frac{\sin(\omega t)}{\sin(\omega t - 2\pi/3)} \quad (4c)$$

$$\frac{i_c}{i_b} = \frac{1-d_2}{d_1+d_2-2} = \frac{\sin(\omega t - 4\pi/3)}{\sin(\omega t - 2\pi/3)}. \quad (4d)$$

$$\begin{bmatrix} r_1\left[\frac{d_1}{2}\left(\frac{N_1+N_2}{N_1}\right)^2+\frac{1-d_1}{2}+\frac{d_2}{2}\left(\frac{N_1+N_2}{N_1}\right)^2+\frac{1-d_2}{2}\right] & \frac{1-d_1}{2} & -\frac{2-d_1-d_2}{2} & \frac{1-d_2}{2} & 0 & 0 & 0 \\ (1-d_1)/2 & 0 & 0 & 0 & -1 & 0 & 0 \\ -(2-d_1-d_2)/2 & 0 & 0 & 0 & 0 & -1 & 0 \\ (1-d_2)/2 & 0 & 0 & 0 & 0 & 0 & -1 \\ 0 & 1 & 0 & 0 & -r_2 & 0 & 0 \\ 0 & 0 & 1 & 0 & 0 & -r_2 & 0 \\ 0 & 0 & 0 & 1 & 0 & 0 & -r_2 \end{bmatrix}$$

$$\times \begin{bmatrix} i_L \\ u_{Cfa} \\ u_{Cfb} \\ u_{Cfc} \\ i_a \\ i_b \\ i_c \end{bmatrix} = \begin{bmatrix} \left(1+\frac{N_2}{N_1}\frac{d_1+d_2}{2}\right)U_{\rm PV} \\ 0 \\ 0 \\ 0 \\ u_a \\ u_b \\ u_c \end{bmatrix}. \quad (3)$$

Set $1-d_1=K\sin(\omega t)=Ke_a\,(K\in(0,1))$, so $1-d_2=K\sin(\omega t-4\pi/3)=Ke_c$, $2-d_1-d_2=K\sin(\omega t-2\pi/3)=Ke_b$. In Interval I, $|\sin(\omega t-2\pi/3)|$ can be expressed by the average value $3/\pi$, so $d_1+d_2\approx 2-K$, (4a) can be simplified as

$$\left(1+\frac{N_2}{N_1}\frac{2-3K/\pi}{2}\right)U_{\rm PV}=K\left[u_a\sin(\omega t)+\frac{u_b}{2}\sin\left(\omega t-\frac{2\pi}{3}\right)+u_c\sin\left(\omega t-\frac{4\pi}{3}\right)\right]+r_1\left[\frac{1}{2}\left(\frac{N_1+N_2}{N_1}\right)^2\left(2-\frac{3K}{\pi}\right)+\frac{3K}{2\pi}\right]i_L \quad (5)$$

the input dc current $I_{\rm PV}$ can be expressed as

$$I_{\rm PV}=\frac{d_1 i_{L1}}{2}+\frac{1-d_1}{2}i_L+\frac{d_2 i_{L1}}{2}+\frac{1-d_2}{2}i_L=\left[1+\left(1-\frac{3K}{2\pi}\right)\frac{N_2}{N_1}\right]i_L \quad (6)$$

assuming that the RMS of output phase current is I_p, the efficiency of the inverter is η, then

$$I_{\rm PV}=3U_pI_p/\left(U_{\rm PV}\eta\right) \quad (7)$$

derived from (6) and (7)

$$i_L=3U_pI_p\Big/\left\{U_{\rm PV}\eta\left[1+\left(1-\frac{3K}{2\pi}\right)\frac{N_2}{N_1}\right]\right\} \quad (8)$$

substituting (1) and (8) into (4a), one can obtain

$$U_p=\frac{U_{\rm PV}\left[1+(N_2/N_1)\,(2-3K/\pi)/2\right]}{\frac{3\sqrt{2}K}{4}+3I_pr_1\frac{[(N_1+N_2)/N_1]^2(2-3K/\pi)/2+3K/(2\pi)}{U_{\rm PV}\eta[1+(N_2/N_1)(1-3K/(2\pi))]}}. \quad (9)$$

Assuming that $r_1=0$, $\eta=100\%$, and the inverter in CCM mode, the ideal VTR $U_p/U_{\rm PV}$ is

$$\frac{U_p}{U_{\rm PV}}=\frac{2\sqrt{2}\left[1+(N_2/N_1)\right]}{3K}-\frac{\sqrt{2}\,(N_2/N_1)}{\pi} \quad (10)$$

where the coefficient K is a constant for certain U_p, $U_{\rm PV}$, and N_2/N_1. To introduce the inner-loop feedback of the energy storage inductor current, set $K=kI_{L\rm avg}$, thus the two-loop control strategy shown in Fig. 2 is obtained. Equation (10) can also be expressed as curves in Fig. 5.

In Fig. 5: 1) for the same N_2/N_1, the larger energy storage duty ratio d_1 and d_2, the smaller energy release duty ratio $1-d_1$, $1-d_2$, the smaller coefficient K is, and the larger the VTR $U_p/U_{\rm PV}$ is; 2) for the same K, the larger N_2/N_1, the larger $U_p/U_{\rm PV}$ is; and 3) when $N_2/N_1=0$, $U_p/U_{\rm pv}=2\sqrt{2}/(3K)$ is the minimum, that is the VTR of the single-stage three-phase current-source PV grid-connected inverter with low VTR. When $U_{\rm PV}=96$ V, $U_p=220$ V, $N_2/N_1=2$, and $K=0.886$. Therefore, the VTR of the proposed inverter can be adjusted by the duty ratio and the center-tapped turns ratio.

C. Steady State of Three-Phase Grid-Connected Current and the Reactive Power Regulated Angle θ

Taking the Interval I as an example, two operating modes of the inverter within the former carrier wave period $T_S/2$ are shown in Fig. 3(a) and (b). Set the initial value of i_L within the former carrier wave period $T_S/2$ is $i_L(0)$, then the final value of i_L is given by

$$i_L\left(\frac{T_S}{2}\right)=\left\{\left[i_L(0)+\frac{U_{\rm PV}}{L_1}d_1\frac{T_S}{2}\right]\frac{N_1}{N_1+N_2}+\frac{U_{\rm PV}-u_{ab}}{L}(1-d_1)\frac{T_S}{2}\right\}\frac{N_1+N_2}{N_1}=i_L(0)+\frac{U_{\rm PV}}{L_1}d_1\frac{T_S}{2}+\frac{U_{\rm PV}-u_{ab}}{L}(1-d_1)\times\frac{T_S}{2}\frac{N_1+N_2}{N_1}. \quad (11)$$

Two operating modes of the inverter within the latter carrier wave period $T_S/2$ are shown in Fig. 3(a) and (c). The final value of i_L is given by

$$i_L(T_S)=\left\{\left[i_L\left(\frac{T_S}{2}\right)+\frac{U_{\rm PV}}{L_1}d_2\frac{T_S}{2}\right]\frac{N_1}{N_1+N_2}+\frac{U_{\rm PV}-u_{cb}}{L}(1-d_2)\frac{T_S}{2}\right\}\frac{N_1+N_2}{N_1}=i_L\left(\frac{T_S}{2}\right)+\frac{U_{\rm PV}}{L_1}d_2\frac{T_S}{2}+\frac{U_{\rm PV}-u_{cb}}{L}(1-d_2)\times\frac{T_S}{2}\frac{N_1+N_2}{N_1} \quad (12)$$

within two carrier wave periods, the variation of i_L is

$$\Delta i_L=i_L(T_S)-i_L(0)=\frac{U_{\rm PV}}{L_1}d_1\frac{T_S}{2}+\frac{U_{\rm PV}-u_{ab}}{L}(1-d_1)\times\frac{T_S}{2}\frac{N_1+N_2}{N_1}+\frac{U_{\rm PV}}{L_1}d_2\frac{T_S}{2}+\frac{U_{\rm PV}-u_{cb}}{L}(1-d_2)\frac{T_S}{2}\frac{N_1+N_2}{N_1}. \quad (13)$$

Substituting (1) and (2) into the aforementioned equation and considering $L/L_1=[(\mathrm{N}_1+\mathrm{N}_2)/\mathrm{N}_1]^2$, $1-d_1=$

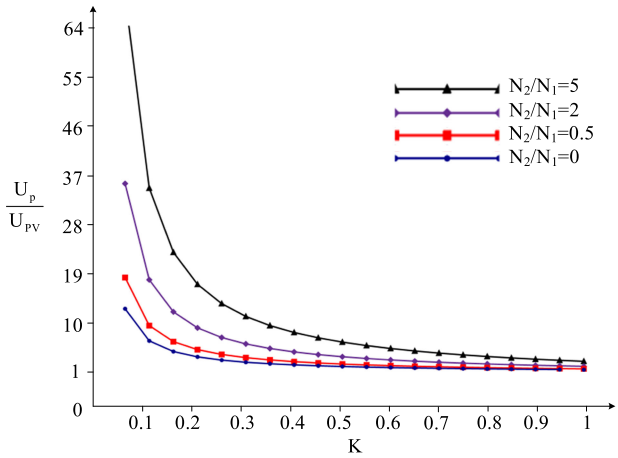

Fig. 5. Related curves between VTR of the proposed inverter with coefficient *K*.

$kI_{L\mathrm{avg}}e_a$, and $1-d_2=kI_{L\mathrm{avg}}e_c$, the variation of i_L is derived as

$$\Delta i_L = \frac{U_{\mathrm{PV}}}{L_1}T_S - \frac{U_{\mathrm{PV}}}{L_1}kI_{L\mathrm{avg}}\left|e_b\right|\frac{N_2}{N_1+N_2}\frac{T_S}{2} - \frac{kI_{L\mathrm{avg}}}{L_1}\frac{3\sqrt{2}}{2}\frac{N_1}{N_1+N_2}\frac{T_S}{2}U_p\cos\theta \tag{14}$$

the magnetizing and demagnetizing of the energy storage inductor basically reach balance within one T_S under steady state. Set $\Delta i_L=0$, derived from the aforementioned equation

$$I_{L\mathrm{avg}} = \frac{2(N_1+N_2)U_{\mathrm{PV}}}{N_2k\left|e_b\right|U_{\mathrm{PV}}+\left(3\sqrt{2}/2\right)N_1kU_p\cos\theta} \tag{15}$$

in Interval I, the average value of $|e_b|=|\sin(\omega t-2\pi/3)|$ can be approximately expressed as $3/\pi$, the aforementioned equation can be simplified as

$$I_{L\mathrm{avg}} = \frac{2(N_1+N_2)U_{\mathrm{PV}}}{3N_2kU_{\mathrm{PV}}/\pi+\left(3\sqrt{2}/2\right)N_1kU_p\cos\theta}. \tag{16}$$

It shows that $I_{L\mathrm{avg}}$ is a constant in steady state.

Within two carrier wave periods, the average value of the filtering capacitor current is approximate to zero, thus the average value of the Phase-a grid-connected current is approximately expressed as

$$i_{a\mathrm{avg}}\approx I_{L\mathrm{avg}}\frac{N_1}{N_1+N_2}\frac{(1-d_1)T_S/2}{T_S}=\frac{N_1}{N_1+N_2}\frac{kI_{L\mathrm{avg}}{}^2}{2}e_a. \tag{17}$$

Similarly, the average value of the Phase-c grid-connected current is approximately expressed as

$$i_{c\mathrm{avg}}\approx I_{L\mathrm{avg}}\frac{N_1}{N_1+N_2}\frac{(1-d_2)T_S/2}{T_S}=\frac{N_1}{N_1+N_2}\frac{kI_{L\mathrm{avg}}{}^2}{2}e_c. \tag{18}$$

Since $i_{a\mathrm{avg}}+i_{b\mathrm{avg}}+i_{c\mathrm{avg}}=0$, one could achieve

$$i_{b\mathrm{avg}}\approx\frac{N_1}{N_1+N_2}\frac{kI_{L\mathrm{avg}}{}^2}{2}e_b \tag{19}$$

$i_{a\mathrm{avg}}$, $i_{b\mathrm{avg}}$, and $i_{c\mathrm{avg}}$ are separately changing with e_a, e_b, and e_c in sinusoidal form, thus the symmetrical three-phase sinusoidal currents are obtained. Derived from (17)–(19), the average three-phase output power is given by

$$P_o = 3U_p\frac{N_1}{N_1+N_2}\frac{kI_{L\mathrm{avg}}}{2\sqrt{2}}I_{L\mathrm{avg}}. \tag{20}$$

The grid-connected current is usually phase lagged caused by the output filter, however, the unity power factor and the reactive power adjustment of the grid can be realized by adjusting angle θ. Taking the Interval I as an example, $\omega t\in(0,\pi/3)$, derived as

$$u_{ab} = \sqrt{2}U_p\sin(\omega t+\theta)-\sqrt{2}U_p\sin(\omega t+\theta-2\pi/3) = \sqrt{6}U_p\cos(\omega t+\theta-\pi/3) \tag{21}$$

$$u_{cb} = \sqrt{2}U_p\sin(\omega t+\theta+2\pi/3)-\sqrt{2}U_p\sin(\omega t+\theta-2\pi/3) = \sqrt{6}U_p\cos(\omega t+\theta) \tag{22}$$

to ensure the normal operating of the CSI, the conditions $u_{ab}>U_{\mathrm{PV}}$ and $u_{cb}>U_{\mathrm{PV}}$ must be met, that is

$$\begin{cases}\sqrt{6}U_p\cos(\omega t+\theta-\pi/3)>U_{\mathrm{PV}}\\ \sqrt{6}U_p\cos(\omega t+\theta)\quad>U_{\mathrm{PV}}.\end{cases} \tag{23}$$

The following equation is derived from the aforementioned equation:

$$\begin{cases}-\arccos\left[U_{\mathrm{PV}}/\left(\sqrt{6}U_p\right)\right]<\omega t+\theta-60^o\\ \qquad<\arccos\left[U_{\mathrm{PV}}/\left(\sqrt{6}U_p\right)\right]\\ -\arccos\left[U_{\mathrm{PV}}/\left(\sqrt{6}U_p\right)\right]<\quad\omega t+\theta\\ \qquad<\arccos\left[U_{\mathrm{PV}}/\left(\sqrt{6}U_p\right)\right].\end{cases} \tag{24}$$

When $U_{\mathrm{PV}}=96$ V and the variation range of the grid voltage is $\pm10\%$, the phase adjusting range of the grid-connected current is $-18.58^\circ<\theta<18.58^\circ$.

IV. Analysis of HF Switching Process

Here, L_{lk1}, L_{lk2} are the leakage inductors of L_1 and L_2, respectively, and C_s and C_{sc} are the junction capacitors of *S* and S_c, respectively, which are much smaller than C_c. S_c operates in the half switching period $T_s/2$ when energy storage time is shorter and after *S* is turned OFF, and the switching frequency of S_c is half of *S*. There are 14 different operating intervals within one HF switching period T_S, the former six operating intervals (t_0–t_6) can be considered as special example of the latter eight ones (t_7–t_{14}). The HF switching process waveforms and the equivalent circuits in the latter eight operating intervals (t_7–t_{14}) of the inverter are shown in Fig. 6.

1) [t_6–t_7]: At t_6, S_{a1} is turned OFF with zero current switching (ZCS). In this interval, L_{lk1}, and L_{lk2} resonate with the equivalent junction capacitor of a bridge arm and i_{L1}, i_{L2}, and u_{dc} damply oscillate. L_1 charges energy via the path of U_{PV}, L_1, and *S*, and i_a, i_b, and i_c are maintained by C_{fa}, C_{fb}, and C_{fc}, respectively.
2) [t_7–t_8]: At t_7, S_{c1} is turned ON; S is still ON to ensure the energy is reliably released in *L*. The operating state of the inverter is similar to interval t_6–t_7.
3) [t_8–t_9]: At t_8, *S* is turned OFF, u_{ds} rapidly increases to u_{Cc} and u_{dsc} rapidly decreases to zero by the energy of L_1, then the parasitic diode of S_c is conducted and u_{ds} is clamped at u_{Cc}. C_c resonates with L_{lk1} and L_{lk2}, the subcircuit current of energy storage switch decreases, i_{L2} increases from zero until meeting the equation $(N_1+N_2)i_{L2}(t_9)=N_1i_{L1}(t_8)$ at t_9. U_{PV} and L_1 deliver power to the grid via the path of L_2, S_{c1}, D_{c1}, L_{fc}, u_c, u_b, L_{fb}, S_{b2}, and D_{b2}, i_a is maintained by C_{fa}.
4) [t_9–t_{10}]: At t_9, S_c is turned ON with zero voltage switching. C_c continues to resonate with L_{lk1} and L_{lk2}, the operating state of this interval is similar to interval t_8–t_9.
5) [t_{10}–t_{11}]: At t_{10}, $i_{Cc}>0$ and S_c is turned OFF, i_{Cc} flows through the parasitic diode of S_c, the operating state of this interval is similar to interval t_9–t_{10}.
6) [t_{11}–t_{12}]: At t_{11}, i_{Cc} decreases to zero, then L_{lk1} and L_{lk2} resonate with C_s, C_c, and C_{sc}, U_{PV} and *L* deliver

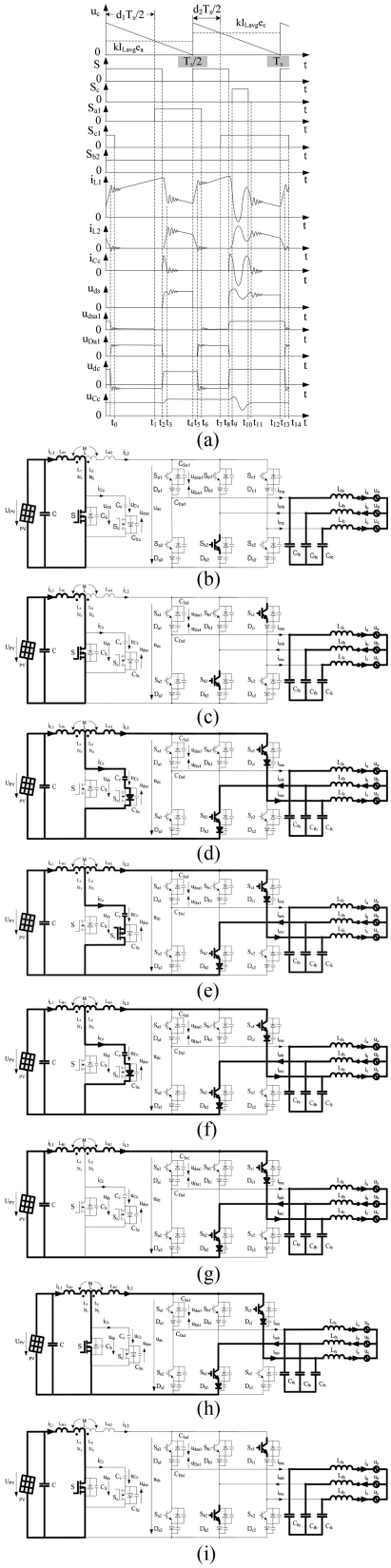

Fig. 6. HF switching process waveforms and equivalent circuits in the operating intervals of the proposed inverter.

power to the grid via the path of S_{c1}, D_{c1}, L_{fc}, L_{fb}, S_{b2}, and D_{b2}, i_a is maintained by C_{fa}.

7) [t_{12}–t_{13}]: At t_{12}, S is turned ON, then L_{lk1} and L_{lk2} make i_{L1} increasing gradually and i_{L2} decreasing gradually until i_{L1} and i_{L2} meet the equation $N_1 i_{L1}(t_{13}) = (N_1 + N_2) i_{L2}(t_{12})$ at t_{13}, $U_{\rm PV}$ and L deliver power to the grid via the path of S_{c1}, D_{c1}, L_{fc}, L_{fb}, S_{b2}, and D_{b2}, i_a is maintained by C_{fa}.
8) [t_{13}–t_{14}]: At t_{13}, i_{L2} decreases to zero, L_{lk1} and L_{lk2} resonate with the equivalent junction capacitor of a bridge arm, i_{L1}, i_{L2}, and u_{dc} damply oscillate. In this interval, L_1 charges energy via the path of $U_{\rm PV}$, L_1, and S, i_a, i_b, and i_c are maintained by C_{fa}, C_{fb}, $C_{\rm fc}$, respectively. At t_{14}, S_{c1} is turned OFF with ZCS, L basically realizes magnetic reset, then the next T_s starts.

The operating state of t_0–t_1 is similar to t_6–t_7, whereas the operating states of t_1–t_2, t_2–t_3, t_3–t_4, t_4–t_5, and t_5–t_6 are, respectively, similar to t_7–t_8, t_8–t_9, t_{11}–t_{12}, t_{12}–t_{13}, and t_{13}–t_{14}, where S_{a1} and S_{b2} are ON. When the inverter is transmitting energy, the active clamped circuit effectively suppresses the turn-off voltage spike of S.

V. Designing Criterion of Center-Tapped Energy Storage Inductor

Taking the first 60° interval as shown in Fig. 2(a) as an example, the duty ratio of the energy storage switch S in a switching period T_s is given by

$$d = d_1 + d_2 = 1 - kI_{L\rm avg}\left(e_a + e_c\right)/2 = 1 - kI_{L\rm avg}\left|e_b\right|/2. \tag{25}$$

Substituting (15) into the aforementioned equation, gives

$$d = 1 - \frac{(N_1 + N_2)U_{\rm PV}\left|e_b\right|}{N_2\left|e_b\right|U_{\rm PV} + 3\sqrt{2}N_1 U_p \cos\theta/2}. \tag{26}$$

Substituting $\cos\theta = 1$, the minimum of $|e_b|$ is $\sqrt{3}/2$, and $d \le 0.7$ into (26), the turns ratio is $N_2/N_1 \ge 1.75$, where $N_2/N_1 = 2$ is chosen.

The following equation is derived from (15):

$$K = kI_{L\rm avg} = \frac{2(N_1 + N_2)U_{\rm PV}}{N_2 U_{\rm PV} + \left(3\sqrt{2}/2\right)N_1 1.1U_p} \tag{27}$$

the peak value of the grid-connected phase current can be derived from (18)–(20) as

$$\sqrt{2}I_p = \frac{N_1}{N_1 + N_2}\frac{KI_{L\rm avg\,max}}{2} = \sqrt{2}\frac{P_o}{3U_p} \tag{28}$$

where $I_{L\rm avgmax}$ is the $I_{L\rm avg}$ corresponded to the peak value of the grid-connected phase current.

The input current ripple under full load is 15%, then

$$\frac{\Delta i_L}{i_L} = \frac{1}{I_{L\rm avg\,max}}\frac{U_{\rm PV}}{L_1}d_{\max}T_s \le 15\% \tag{29}$$

$L_1 \ge$ 0.068 mH, L_1 is chosen 0.068 mH, and $L = 0.612$ mH.

The high flux iron silicon core of PHD60 is selected, where the effective length of magnetic circuit $l_e = 34$ cm, with core cross-sectional area $S = 4$ cm^2. Designed according to the permeability

under peak current dropping to 50% of the initial permeability, the winding turn number of L_1 is

$$N_1 = \sqrt{\frac{L_1 le \times 10^8}{0.4\pi(50\%\mu)3S}} = \sqrt{\frac{0.068 \times 10^{-3} \times 34 \times 10^8}{0.4 \times 3.1416 \times (50\% \times 60) \times 12}} = 22.6\,(T)\,. \tag{30}$$

Thus, $N_1 = 24$ T is selected and $N_2 = 48$ T.

VI. Prototype Experiments

The parameters of the designed prototype are as follows: rated output power 3 kW, rated voltage of PV cells $U_{\rm PV} = 96$ V, output three-phase ac voltage 380V50HzAC, switching frequency $f_s = 60$ kHz/30 kHz, current sampling frequency 60 kHz, max duty ratio $d_{\max} = 0.7$, energy storage inductor $L = 0.612$ mH $(N_2/N_1 = 48/24)$ using high flux iron silicon core of PHD60, output filtering capacitor $C_f = 7.9$ μF, output filtering inductor $L_f = 0.6$ mH, and clamping capacitor $C_c = 0.44$ μF. MOSFET IXFX98N50P3 for *S*, MOSFET IXFK64N50P for S_c, IGBT IXYH60N90C3 for $S_{a1} - S_{c2}$, DSEI30-10A for $D_{a1} - D_{c2}$, S25P150D15Y, S26P200D15Y, and S25P100D15Y for the current sensor, TMS320F28335DSP for the control circuit chip, and Chroma TC.P.32.200.400.S for the PV power simulator, while the MPPT employs the open circuit voltage and disturbance observation method [18].

The open circuit voltage of the PV power simulator is set at 112.4 V, the short-circuit current 37.05 A, the MPP voltage 96.2 V, the MPP current 34.75 A, and the MPP power 3430 W. In order to obtain switching overlap, the relevant power switches are turned OFF with delay by dead-band generator in the DSP. The designed prototype experimental results of the 3-kW single-stage three-phase current-source PV grid-connected inverter with high VTR under the setting MPP condition are shown in Fig. 7. The experimental results have shown that:

1) the waveforms of the energy storage inductor current i_{L1} and i_{L2} and their HF expanded waveforms are shown in Fig. 7(a) and (b), which indicate L_{lk1} and L_{lk2} resonate with C_s and $C_{\rm sc}$ or the equivalent junction capacitor of the bridge arm;
2) the drive signal $u_{\rm gs}$ and drain–source voltage $u_{\rm ds}$ of *S* and their HF expanded waveforms are shown in Fig. 7(c) and (d), which indicate the envelope of $u_{\rm ds}$ is the superposition of dc component and the corresponding output line voltage wave;
3) the drive signal $u_{\rm gsc}$ and the drain–source voltage $u_{\rm dsc}$ of S_c and their HF expanded waveforms are shown in Fig. 7(e) and (f), which indicate that its switching frequency is half of *S*, and the oscillation is caused by the resonance between L_{lk1}, L_{lk2}, and C_c;
4) the clamping capacitor voltage u_{Cc} and its HF expanded waveforms are shown in Fig. 7(g) and (h), which indicate u_{Cc} withstands the drain–source voltage spikes of S;

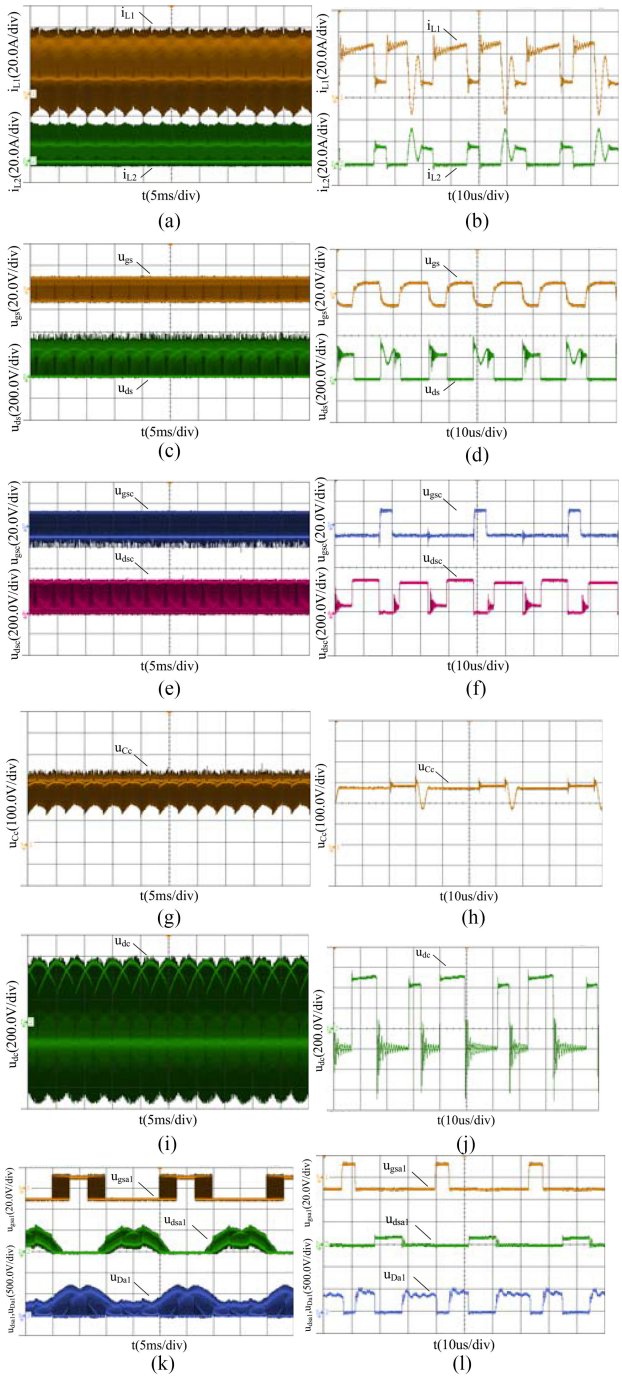

Fig. 7. Continued.

5) the dc voltage $u_{\rm dc}$ of the bridge arm and its HF expanded waveforms are shown in Fig. 7(i) and (j), which indicate the envelope of $u_{\rm dc}$ differs to its corresponding line voltage;
6) the drive signal, the drain–source voltage of the energy release switches, and the voltage of the blocking diodes in the bridge arm along with their HF expanded waveforms in different intervals are shown in Fig. 7(k)–(r), which indicate the waveforms of the upper and lower bridge arm are not completely symmetrical;

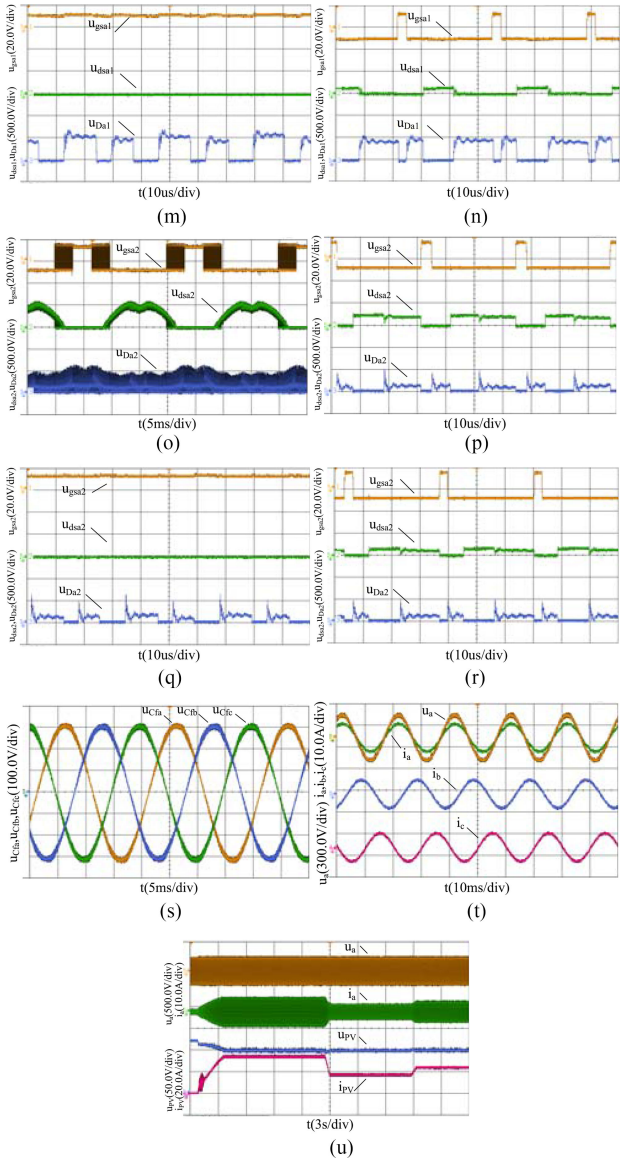

Fig. 7(a). Experimental waveforms of the inverter under setting MPP condition. (a) Energy storage inductance current i_{L1}, i_{L2}. (b) HF expanded of i_{L1}, i_{L2}. (c) Drive signal u_{gs} and drain-source voltage u_{ds} of S. (d) HF expanded of u_{gs}, u_{ds}. (e) Drive signal u_{gsc} and drain–source voltage u_{dsc} of S_c. (f) HF expanded of u_{gsc} u_{dsc}. (g) Clamping capacitance voltage u_{Cc}. (h) HF expanded of u_{Cc}, (i) DC side voltage u_{dc} of the bridge arm. (j) HF expanded of u_{dc}. (k) Drive signal u_{gsa1}, drain-source voltage u_{dsa1} of S_{a1} and voltage u_{Da1} of D_{a1} (l) HF expanded of u_{dsa1}, u_{gsa1}, and u_{Da1} in Interval I. (m) HF expanded of u_{dsa1}, u_{gsa1}, and u_{Da1} in Interval II. (n) HF expanded of u_{dsa1},u_{gsa1}, and u_{Da1} in Interval III. (o) Drive signal u_{gsa2}, drain-source voltage u_{dsa2} of *Sa2* and voltage u_{Da2} of D_{a2}. (p) HF expanded of u_{dsa2}, u_{gsa2}, and u_{Da2} in Interval IV. (q) HF expanded of u_{dsa2}, u_{gsa2}, and u_{Da2} in Interval V. (r) HF expanded of u_{dsa2},u_{gsa2}, and u_{Da2} in Interval VI. (s) Output filter capacitance voltage u_{Cfa}, u_{Cfb}, u_{Cfc}. (t) Three-phase grid-connected current i_a, i_b, i_c and Phase-a grid voltage u_a. (u) Dynamic tracking MPPT waveforms.

7) the voltage of the output filter capacitor are shown in Fig. 7(s), which indicates a good symmetry of three-phase filter capacitor voltage;
8) the waveforms of the three-phase grid-connected current and phase-*a* grid voltage are shown in Fig. 7(t), which indicate the three-phase grid-connected current waveforms have a high quality and are in phase of the grid voltage, with a current total harmonic distortion (THD) 2.68%;
9) the dynamic tracking MPPT waveforms under start-up and light intensity change are shown in Fig. 7(u), which indicate the system achieves its MPP after 3 s with fast MPPT tracking speed, high stability, and smooth PV output current i_{PV}, meanwhile the grid-connected current i_a can quickly be tracked in the abrupt process of light intensity from 1000 W/m^2 $\rightarrow$ 500 W/m^2 $\rightarrow$ 700 W/m^2.

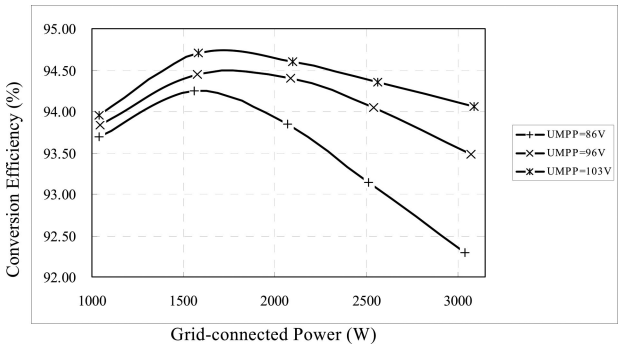

Fig. 8. Conversion efficiency curves of the proposed inverter.

The conversion efficiency curves of the proposed three-phase PV grid-connected inverter under three different MPP voltages of PV cells 86, 96, and 103 V is shown in Fig. 8. The efficiency under rated grid-connected power of 3 kW is, respectively, 92.29%, 93.48%, and 94.06%, with a maximum efficiency, respectively, 94.25%, 94.50%, and 94.75% around 1500 W. Especially, the conversion efficiency is up to 95.34% when $U_{\mathrm{MPP}} = 110$ V. The main loss of the inverter includes power switch and blocking diodes losses and the iron loss, copper loss of the energy storage inductor. The inherent loss dominates under less grid-connected power, but the conduction loss of power switches and blocking diodes and the copper loss of the energy storage inductor dominates under larger grid-connected power. When U_{MPP} rises, $I_{L\mathrm{avg}}$ and the inverter loss decrease, thus the conversion efficiency increases. With the development of the bidirectional blocking power device such as the reverse-blocking IGBT, the power switches of the current mode inverter will be not necessary to be connected with serial reverse blocking diodes, and the conversion efficiency will be further improved. The future work the authors expect to do is to investigate the three-phase PV off-grid inverter with energy storage element.

An phase PWM three-phase CSI proposed in [12] has the following performance: the output power is only 1.92 kW, the energy storage inductors is as high as 20 mH, the output filter is large as 15 μF and 3mH, the VTR is only 2.97, and the conversion efficiency and THD of the output waveform are not given. An instantaneous current value feedback controlled three-phase PV CSI proposed in [13] has the following performance: the conversion efficiency is only 83.61% for 3-kW output power, the VTR is only 1.14, the output filter is large as 10 μF and 2.3 mH, and the energy storage inductor value and THD of the grid-connected current waveform are not given.

A grid-connected current dynamic prediction optimization controlled three-phase PV CSI proposed in [14] has the following performance: the output power is only 2.03 kW, energy storage inductor value is as high as 15 mH, the VTR is only 1.61, the output waveform THD is 5.0%, and the conversion efficiency is not given. The three-phase CSI discussed in [15] has the following performance: the output power is only 2.0 kW, the energy storage inductor is as high as 10 mH, and the output filter is large as 20 μF and 7.5 mH, the VTR is 3.2, the output waveform THD is 5.0%, and the conversion efficiency is not given. A modified single-stage three-phase CSI presented in [16] has the following performance: the output power is only 0.5 kW, the VTR is 2.0, the output waveform THD is 4.5%, and the conversion efficiency and THD of the output waveform are not given. A single-stage CSI proposed in [17] has the following performance: the output power is only 2.0 kW, the energy storage inductor is as high as 10 mH, the VTR is 3.2, the output inductor filter is large as 20 mH, the output waveform THD is 4.1%, and the conversion efficiency is not given. The two-stage three-phase current/voltage source PV inverters discussed in [19] and [20] have the following performance: the energy storage inductor is as high as 2.42 or 3.0 mH, the VTR is 0.99 or 0.95, the output filter is large as 5 μF and 6 or 5 mH, and the second conversion efficiency is 90.94%, and THD of the output waveform is not given. Comparison results show that the proposed inverter has the excellent performances, namely, higher VTR, much smaller energy storage inductor and higher conversion efficiency. Moreover, it has lower output current THD than that of [12]–[17] and [20] and smaller output CL filter than that of [12]–[13], [15]–[17], and [19]–[20], yet it has larger output power than that of [12], [14]–[17], and [20]. When the turns ratio N_2/N_1 of *L* is larger, the proposed inverter will have higher VTR. While lower PV voltage can be single-stage boosted and inverted into the rated grid voltage, the voltage configuration of the PV cells is flexible, which is the major achievement in this paper compared to current PV inverters from peers.

VII. Conclusion

1) The circuit topology of the proposed inverter is a sequentially cascaded of the input filter capacitor, the center-tapped energy storage inductor, three-phase inverting bridge with six serial blocking diodes, and output *CL* filter, with an energy storage switch connected between the center tap of *L* and the negative end of the input source.
2) The proposed two-loop improved zone SPWM control strategy can ensure the normal operation of the CSI in any HF switching period with the condition that output line voltage are not smaller than input voltage, i.e., $\sqrt{6}/2\mathrm{U}_p \geq \mathrm{U}_{\mathrm{PV}}$, and the reactive power adjustment of the system is realized.
3) There are six operating intervals in one output line frequency period, each operating interval has three operating modes; the VTR expression is derived, which can be adjusted through the coefficient $K = kI_{L\mathrm{avg}}$ and the turns ratio N_2/N_1 of *L*.
4) The active clamped subcircuit can effectively suppress the turn-off voltage spike of *S* caused by the leakage inductor, and there are 14 different operating intervals within one HF switching period T_s.
5) The design criterion of the center-tapped energy storage inductor is derived.
6) The designed 3-kW 96VDC/380V50Hz3φAC PV grid-connected inverter prototype has excellent performances such as higher VTR, much smaller energy storage inductor and higher conversion efficiency, and the experimental results validate theoretical analysis.

References

[1] T. K. S. Freddy, N. A. Rahim, W. P. Hew, and H. S. Che, "Modulation techniques to reduce leakage current in three-phase transformerless H7 photovoltaic inverter," *IEEE Trans. Ind. Electron.*, vol. 62, no. 1, pp. 322–331, Jan. 2015.

[2] T. Messo, J. Jokipii, J. Puukko, and T. Suntio, "Determining the value of DC-link capacitor to ensure stable operation of a three-phase photovoltaic inverter," *IEEE Trans. Power Electron.*, vol. 29, no. 2, pp. 665–673, Feb. 2014.

[3] J. Ji *et al.*, "A simple differential mode EMI Suppressor for the LLCL-filter-based single-phase grid-tied transformerless inverter," *IEEE Trans. Ind. Electron.*, vol. 62, no. 7, pp. 4141–4147, Jul. 2015.

[4] I. Serban, "Power decoupling method for single-phase H-bridge inverters with no additional power electronics," *IEEE Trans. Ind. Electron.*, vol. 62, no. 8, pp. 4805–4813, Aug. 2015.

[5] B. Singh, C. Jain, and S. Goel, "ILST control algorithm of single-stage dual purpose grid connected solar PV system," *IEEE Trans. Power Electron.*, vol. 29, no. 10, pp. 5347–5357, Oct. 2014.

[6] D. Barater, G. Buticchi, E. Lorenzani, and C. Concari, "Active common-mode filter for ground leakage current reduction in grid-connected PV converters operating with arbitrary power factor," *IEEE Trans. Ind. Electron.*, vol. 61, no. 8, pp. 3940–3950, Aug. 2014.

[7] L. S. Garcia *et al.*, "Modeling and control of a single-stage current source inverter with amplified sinusoidal output voltage," in *Proc. IEEE Appl. Power Electron. Conf.*, 2012, pp. 2024–2031.

[8] R. T. H. Li, H. S. H. Chung, and T. K. M. Chan, "An active modulation technique for single-phase grid-connected CSI," *IEEE Trans. Power Electron.*, vol. 22, no. 4, pp. 1373–1382, Jul. 2007.

[9] D. Chen, Y. Qiu, Y. Chen, and Y. He, "Nonlinear PWM-controlled single-phase boost mode grid-connected photovoltaic inverter with limited storage inductance current," *IEEE Trans. Power Electron.*, vol. 32, no. 4, pp. 2717–2727, Apr. 2017.

[10] B. N. Alajmi, K. H. Ahmed, G. P. Adam, and B. W. Williams, "Single-phase single-stage transformer less grid-connected PV system," *IEEE Trans. Power Electron.*, vol. 28, no. 6, pp. 2264–2676, Jun. 2013.

[11] D. Chen and Y. Chen, "Step-up AC voltage regulators with high-frequency link," *IEEE Trans. Power Electron.*, vol. 28, no. 1, pp. 390–397, Jan. 2013.

[12] M. Saghaleini and B. Mirafrazl, "Reactive power control in three-phase grid-connected current source boost inverter," in *Proc. IEEE Appl. Power Electron. Conf.*, 2012, pp. 904–910.

[13] A. Kavimandan and S. P. Das, "Control and protection strategy for a three-phase single-stage boost type grid-connected current source inverter for PV applications," in *Proc. IEEE Int. Conf. Ind. Technol.*, 2013, pp. 1722–1727.

[14] Y. Li, P. Li, Y. Chen, and D. Zhang, "Single-stage three-phase current-source inverter for photovoltaic grid-connected system," in *Proc. 16th Eur. Conf. Power Electron. Appl.*, 2014, pp. 1–9.

[15] A. Singh, A. K. Kaviani, and B. Mirafzal, "On dynamic models and stability analysis of three-phase phasor PWM-based CSI for stand-alone applications," *IEEE Trans. Ind. Electron.*, vol. 62, no. 5, pp. 2698–2707, May 2015.

[16] B. Eskandari and M. T. Bina, "Support vector regression-based distortion compensator for three-phase DC-AC boost-inverters: Analysis and experiments," *IET Trans. Power Electron.*, vol. 7, no. 2, pp. 251–258, Feb. 2014.

[17] A. Singh, A. A. Milani, and B. Mirafzal, "Modified phasor pulse width modulation method for three-phase single-stage boost inverter," in *Proc. IEEE Appl. Power Electron. Conf.*, 2014, pp. 1276–1280.

[18] C. C. Hua, W. T. Chen, and Y. H. Fang, "A hybrid MPPT with adaptive step-size based on single sensor for photovoltaic systems," in *Proc. Int. Conf. Inf. Sci. Electron. Elect. Eng.*, 2014, pp. 441–445.
[19] C. Jain and B. Singh, "A three-phase grid tied SPV system with adaptive DC link voltage for CPI voltage variations," *IEEE Trans. Sustain. Energy*, vol. 7, no. 1, pp. 337–344, Jan. 2016.
[20] M. C. Cavalcanti, F. Bradaschia, P. E. P. Ferraz, and L. R. Limongi, "Two-stage converter with remote state pulse width modulation for transformerless photovoltaic systems," *Elect. Power Syst. Res.*, vol. 108, no. 3, pp. 260–268, Mar. 2014.

Daolian Chen (SM'08) was born in Fujian, China, in 1964. He received the B.S., M.S., Ph.D. degrees and Postdoctoral Certification from the Department of Electrical Engineering, Nanjing University of Aeronautics and Astronautics (NUAA), Nanjing, China, in 1986, 1989, 1998, and 2001, respectively.

He was a Teaching Assistant, a Lecturer, an Associated Professor, and a Professor with the Department of Electrical Engineering, NUAA, in 1989, 1991, 1996, and 2002, respectively. He has been a Professor with the College of Electrical Engineering, Fuzhou University, Fuzhou, China, since 2005. He has been a "National Class Expert of the Hundred, Thousand, and Ten Thousand Talent Project," "Delta Scholar," and "National outstanding professional and technical personnel", China, since 2009, 2014, and 2014. He has been a Director of the Fujian Key Laboratory of New Energy Generation and Power Conversion, Fuzhou University, since 2015. He has published three works and more than 100 technical papers. He is the holder of 20 invention patents. His research interests include power electronics conversion, new energy source generating, and aviation electrical power supply systems.

Dr. Chen received one national and three province class reward productions of science and technology.

Jiahui Jiang was born in Fujian, China, in 1989. He received the B.S. degree from the College of Electrical Engineering, Fuzhou University, Fuzhou, China, in 2012, where he is currently working toward the Ph.D. degree with the Fujian Key Laboratory of New Energy Generation and Power Conversion.

He has published several technical papers. His research interests mainly include new energy source generating system.

Yanhui Qiu was born in Fujian, China, in 1988. He received the B.S. degree from the College of Electrical Engineering, Fuzhou University, Fuzhou, China, in 2011, where he is currently working toward the Ph.D. degree with the Fujian Key Laboratory of New Energy Generation and Power Conversion.

He has published several technical papers. His research interests mainly include new energy source generating system.

Jie Zhang was born in Fujian, China, in 1987. She received the B.S. degree from the College of Electrical Engineering, Fuzhou University, Fuzhou, China, in 2010, where she is currently working toward the Ph.D. degree with the Fujian Key Laboratory of New Energy Generation and Power Conversion.

She has published several technical papers. Her research interests mainly include new energy source generating system.

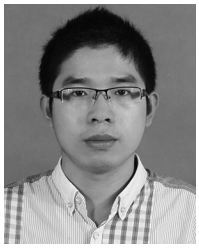

Fusong Huang was born in Fujian, China, in 1989. He received the B.S. and M.S. degrees in electrical engineering from Fuzhou University, Fuzhou, China, in 2011 and 2014, respectively.

He is currently an Engineer in Silergy Technology, Inc., Ltd., Hangzhou, China. He has published several technical papers. His research interests mainly include high-frequency power conversion.